Applied Physics A (2022) 128:515
https://doi.org/10.1007/s00339-022-05655-1

Applied Physics A
Materials Science & Processing

Structural, optical and electrical properties of copper (Cu) and [nickel (Ni), copper]: co-doped SnO_2 nanoparticles prepared by sol–gel method

Wegene Lema Lachore[1] · Dinsefa Mensur Andoshe[3] · Fekadu Gashaw Hone[2] · Mulualem Abebe Mekonnen[1]

Received: 14 March 2022 / Accepted: 30 April 2022 / Published online: 21 May 2022

Abstract
In this work, the un-doped, Cu-doped, and (Ni, Cu) co-doped SnO_2 nanoparticles (NPs) were synthesized using the sol–gel method with a fixed concentration of copper dopant while varying the nickel concentrations. The structural, optical and electrical properties, as well as the surface morphology, were investigated systematically by various characterization techniques. The X-ray diffraction (XRD) study confirmed that the prepared samples had a tetragonal rutile crystal structure for all single-doped/co-doped and un-doped SnO_2 NPs. The XRD results further confirmed that the crystalline sizes varied from 16 to 10 nm with the concentrations of the dopants. The UV–Vis diffusion reflectance spectroscopy (DRS) analysis showed that the optical band gap was found to be decreased from 3.38 to 3.27 eV when the dopant concentrations were increased. The energy dispersive analysis of X-ray spectra (EDX) results confirmed the presence of the expected elements in the prepared samples. Three major photoluminescence (PL) emission peaks were observed in the visible region, with a small shift toward lower wavelengths with dopant and co-dopant concentrations. Chemical bonding and the position of the O–Sn–O bond at 600–660 cm^{-1} were confirmed by the Fourier transform infrared spectroscopy (FTIR) study. The activation energies and conduction mechanisms of the prepared samples were investigated using the Hall Effect measurement method. The I–V studies confirmed that the prepared samples had a good ohmic contact behavior and the resistivity decreased significantly for co-doped sample.

Keywords Sol–gel method · SnO_2 NPs · Co-dopant · Activation energies · Hall Effect

1 Introduction

Transition metal oxide semiconductor nanomaterials, such as titanium dioxide (TiO_2), tin dioxide (SnO_2), zinc oxide (ZnO), copper oxide (CuO), and tungsten trioxide (WO_3), have been extensively investigated due to their potential applications in a variety of disciplines, including catalysis, spintronic devices, nanoelectronics, storage devices, and photonic devices [1]. For instance, SnO_2 is an n-type semiconductor with a broad optical band gap and excellent electrical, catalytic, optical, and thermal stability [1, 2]. This semiconductor material has a tetragonal rutile crystalline structure with band gap energy of about 3.6 eV [3]. It has got a lot of interest because of its well-balanced chemical, electrical, and optical properties [4]. Therefore, it has been widely used in various applications such as photovoltaic cells [5], optoelectronic devices [6], transparent conducting electrodes [7, 8], gas sensors [9, 10], photocatalysis [11], etc. The most significant step in improving the optical and electrical properties of SnO_2 NPs is doping. This has the potential to substantially alter its physiochemical properties. Hence, the optical properties of tin dioxide will be improved. SnO_2 NPs have been synthesized using a variety of techniques, including hydrothermal [12, 13], sol–gel [14, 15], co-precipitation [16, 17], microwave [18], and solid-state reaction [10]. The sol–gel approach is a straightforward, cost-effective, and low-temperature method for achieving

✉ Fekadu Gashaw Hone
fekeye@gmail.com

[1] Faculty of Materials Science and Engineering, Jimma Institute of Technology, Jimma University, P. O. Box: 1041, Jimma, Ethiopia

[2] Department of Physics, Addis Ababa University, P.O. Box: 1176, Addis Ababa, Ethiopia

[3] Department of Materials Science and Engineering, Adama Science and Technology University, P. O. Box 1888, Adama, Ethiopia

improved homogeneity in nanoparticle preparation [19]. The properties of SnO_2 NPs are influenced by synthesis parameters such as pH, duration, temperature, and reactant concentrations [20]. These parameters indicate that SnO_2 NPs have different shapes, sizes, and optical properties [21]. Various studies have been conducted using transition metals such as iron (Fe), aluminum (Al), manganese (Mn), cobalt (Co), Cu, Ni, Zn etc. doped into SnO_2 NPs to enhance their properties [22–27]. Cu and Ni, in particular, have outstanding optoelectronic and magnetic properties, so they can significantly improve the possible applications of SnO_2 NPs [28]. For instant, Divya et al. [28] used the co-precipitation approach to make Cu and Ni-doped SnO_2 NPs, and the saturation magnetization and electrical characteristics of the doped samples were improved. Basyooni et al. [29] synthesized a cobalt-doped SnO_2 thin film and discovered that the doped samples' gas sensing characteristics were improved. The influence of co-doping transition metal ions on the structural, optical, electrical, magnetic, and morphological properties of SnO_2 NPs has recently been documented in several published articles; such as Fe-Cu [30], Ni-Mn [31], Fe-Co [32], Fe-Al [33], and F-Ni [34].

Mehraj et al. [32] have investigated the electrical and magnetic properties of Fe and Co co-doped SnO_2 nanostructures synthesized by the citrate-gel method. The obtained results show that the electrical and ferromagnetic behaviors were increased by increasing the Co-and Fe-doping concentrations. Naseem Ahmad N, and Khan S. [35] have reported on the structural, morphological, optical, photoluminescence and electrical properties of Mn and Mn-Co-doped SnO_2 NPs synthesized using the co-precipitation technique, and the optical band gap and activation energy increase with increasing concentration of Co. Duhan et al. have reported ferromagnetism at room temperature in (Cr and Fe) doped SnO_2 NPs prepared by the sol–gel method and discovered that the presence of ferromagnetism in modified SnO_2 NPs was primarily due to the creation of oxygen vacancies due to ionic radii differences between the host and dopants [36]. Ramarajan et al. [37] investigated the optical and electrical properties of Ba and Sb doped SnO_2 thin films prepared by the spray pyrolysis method for the application of transparent conducting electrodes and found that optical transparency and electrical conductivity of co-doped samples were enhanced. Despite the fact that co-doping gives a flexible way to alter the bulk properties of SnO_2 to open up a new door for various optoelectronic applications, a detailed experimental study on the influence of (Cu,Ni) co-doped on the structural, electrical and optical properties of SnO_2 is still missing. To the best of our knowledge, no research groups have looked into the effects of (Cu, Ni) co-doping on the physical properties SnO_2NPs by fixing the concentration of Cu dopant while varying the Ni concentrations. In the present work, we have successfully synthesized doped/co-doped SnO_2 NPs using a cost-effective sol–gel approach. The obtained results provide a good understanding of single-doping and co-doping effects on the structural, optical and electrical properties of SnO_2-based nanomaterials. Moreover, the results revealed that Cu-Ni co-doping is another approach to tune the physical properties of SnO_2 for various optoelectronic applications.

2 Experimental procedure

2.1 Synthesis of un-doped, singly and co-doped (Cu, Ni) SnO_2 NPs

Un-doped, 5% Cu: SnO_2 (singly) and (1% Ni + 5% Cu):SnO_2, (3% Ni + 5%Cu):SnO_2, 5% (Ni,Cu) co-doped SnO_2 NPs were synthesized using the sol–gel method. Stannous chloride dihyrate ($SnCl_2.2H_2O$), copper (II) nitrate trihydrate (Cu $(NO_3)_2.3H_2O$), and nickel (II) nitrate hexahydrate (Ni $(NO_3)_2.6H_2O$) were employed as precursors in the synthesis process, while aqueous NH_4OH used to adjust the pH of the solution. In a typical process, 100 mL of deionized water was used to dissolve 0.18 Mof stannous chloride dihyrate ($SnCl_2.2H_2O$). In a closed-necked flask, the solution was vigorously stirred for 30 min with a magnetic stirrer. After 30 min, a certain amount of aqueous ammonia (25%) which was dissolved in 50 ml deionized water added drop wise to the produced solution with steady magnetic stirring until the pH was close to nine and then stirred for 2 h at 50 °C. After being aged for 16 h, the solution was centrifuged several times with distilled water and ethanol to remove excess ammonia and chloride ions. The gel was dried overnight in an electric oven at 80 °C. After annealing the produced samples at 600 °C for two hours, SnO_2 NPs were generated. Copper (II) nitrate trihydrate and nickel nitrate hexahydrate were added into stannous chloride dihyrate ($SnCl_2$. $2H_2O$) solutions at the same time for the manufacture of singly doped and co-doped with fixed copper (II) nitrate trihydrate (5wt %) and varying nickel (II) nitrate hexahdrate ($X = 1$wt%, 3wt%, 5wt %). The rest of the procedures were usually the same as the ones listed above. The resulting un-doped, singly doped and co-doped samples of nanopowders were used for further characterizations.

2.2 Characterization techniques

The structural analysis carried out by Shimadzu -7000 X- ray diffractometer with CuKα ($\lambda = 1.5406$ Å) radiation at room temperature. The presence of various functional groups in the sample was determined using FTIR spectrophotometer. The surface morphology and elemental composition of the sample were examined using scanning electron microscopy (SEM) and EDAX. UV–Vis DRS was used to make optical

measurements in the wavelength range of 200–800 nm (Model: UV-3600 Plus). PL spectra were performed by HORIBA FluoroMax-4 Spectrofluorometer in the excitation wavelength of 325 nm. The sheet resistance and temperature-dependent electrical conductivity were carried out by the four probe Hall Effect measurement method (model No. HMS 5300) and the current–voltage characteristics of the junctions were measured using a Keithley source meter unit (model 2400) in the dark at room temperature.

3 Results and discussion

3.1 XRD analysis

The XRD pattern for un-doped, singly doped, and co-doped samples is shown in Fig. 1a–e. All of the prominent diffraction peaks in un-doped, singly doped, and co-doped samples exhibit a well-defined tetragonal SnO_2 rutile structure with space group P42/mnm. They agreed exactly with the tetragonal structure of SnO_2 (ICDD-PDF card number 041–144, lattice parameter $a=b=4.7382$, and $c=3.1871$). All the diffraction peaks are very sharp and strong, which indicates the high crystalline nature of SnO_2 NPs. From Fig. 1a–e, it was observed that there were no secondary peaks matching the dopant elements or any other impurities. This indicates that the dopant Cu^{2+} and Ni^{2+} ions are properly substituted into the SnO_2 lattice sites through the sol–gel synthesis method [38]. The intensity of the predominant peak was reduced in singly doped and co-doped samples compared to un-doped samples, as shown in Fig. 1a–e. Therefore, doping caused a defect in the lattice sites that hindered the crystal growth [39]. From Fig. 1f, the diffraction peak small shifts in the plane (110) are observed for singly doped and co-doped samples as compared to un-doped. When increasing the percentage of Ni co-doping in SnO_2, the diffraction peak position moves to a higher 2θ angels. These diffraction peak shifts indicate that the doped Cu^{2+} ions and Ni^{2+} ions are incorporated into the SnO_2 lattice network [28]. Other structural parameters like lattice parameters and volume of unit cells are displayed in Table 1. From Table 1, it was observed that as we move from un-doped

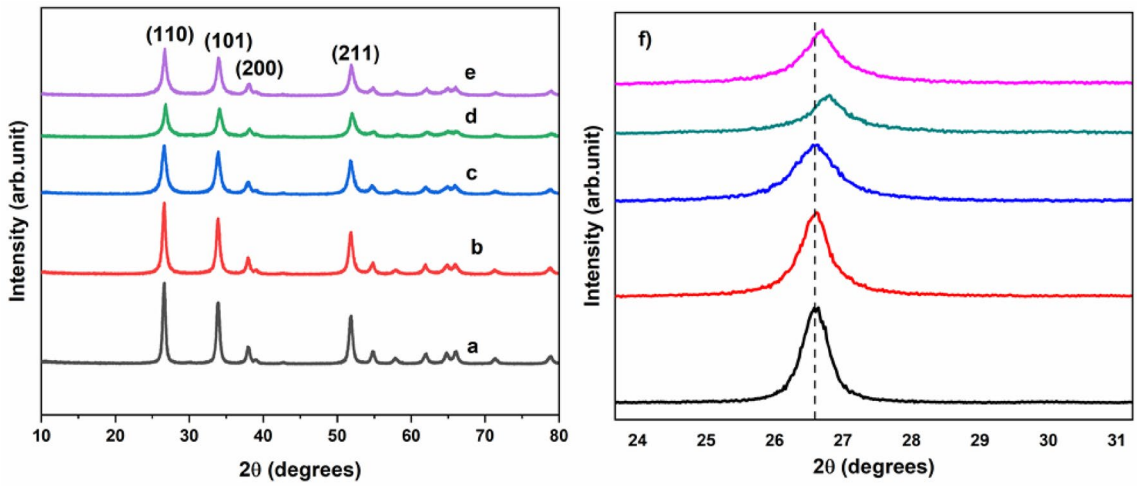

Fig. 1 The XRD patterns (**a**) Un-doped, **b** 5% Cu:SnO_2, **c** (1% Ni + 5%Cu):SnO_2, **d** (3% Ni + 5% Cu):SnO_2, **e** 5% (Cu,Ni):SnO_2NPs. **f** Magnified XRD diffraction peak shift in plane (110) of un-doped, singly and co-doped samples

Table 1 From XRD pattern of the average crystalline size, dislocation density, micro-strain, lattice parameter and volume of unit cell SnO_2 NPs

Concentration	Average crystalline size (nm)	Dislocation density($\times 10^3$(nm^2))	Mircostrain ($\times 10^{-3}$)	Calculated lattice parameter value (Å)		Volume of unit cell $v=a^2c$ (Å)^3
				$a=b$	c	
SnO_2	16	3.6573	8.1104	4.7315	3.1839	71.38
5% Cu:SnO_2	15	4.3160	8.8026	4.7335	3.1836	71.44
(1% Ni + 5% Cu):SnO_2	10	8.8780	12.6982	4.7326	3.1854	71.38
(3% Ni + 5% Cu):SnO_2	12	6.9105	11.0838	4.6987	3.1655	70.41
5% (Ni,Cu):SnO_2	11	7.0525	11.2522	4.7177	3.1752	70.95
JCPDS (41–1445)				4.7382	3.1871	71.55

samples to singly doped and co-doped samples, the lattice parameters "*a*" and "*c*" and the cell volume slightly change. These changed lattice parameters and the cell volume due to the smaller ionic radius of Ni^{2+} (0.69) ions and the larger ionic radius of Cu^{2+} (0.73) ions are easily occupied by the Sn^{4+} (0.71) ions in the synthesized SnO_2 crystal lattice [30, 40–42]. The average crystallite size (*D*) of un-doped, singly doped, and co-doped samples was calculated from (110) and (101) planar orientation using the Debye Scherer relation given in Eq. (1) [43].

$$D = \frac{K\lambda}{\beta \cos\theta} \tag{1}$$

Here, *D* is average crystallite size obtained from the two dominant peaks, *K* is constant for the shape factor equal to 0.9, and λ is the wavelength of X-ray used (CuKα, 0.15406 nm), β is the full width at half maximum of two dominant peaks, and θ is the angel of diffraction of two dominant peaks. The estimated average crystalline size was 16 nm, 15 nm and 10 nm for un-doped, singly doped and co-doped samples respectively (see Table 1). The reduction in crystallite size with singly doped and co-doped is due to differences in the ionic radii of the host and dopants. Furthermore, the incorporation of Cu^{2+} and Ni^{2+} ions into the SnO_2 lattice site results in the suppression of nucleation and subsequent growth of SnO_2 NPs due to the creation of Sn/Cu/Ni or oxygen vacancies [44]. Doping metal, on the other hand, causes faults like oxygen vacancies and tin interstitials.

From the XRD results, the lattice parameters was estimated using Equation (2).

$$\frac{1}{d_{hkl}^2} = \frac{h^2 + k^2}{a^2} + \frac{l^2}{c^2} \tag{2}$$

where *h*, *k* and *l* are Miller indices, d_{hkl} is *d*—spacing give by the Bragg's law equation ($n\lambda = 2d_{hkl}\sin(\theta_{hkl})$. n is order of diffraction equal to one, λ and θ are wavelegth of the incdient beam and Bragg diffraction angle. The defect quantity in the crystal structure of SnO_2 NPs is measured by the dislocation density (δ).

The number of intercepted positions by the dislocation lines per unit area in the plane perpendicular to the dislocation lines (lines/m^2) is also defined [45, 46]. The dislocation density is inversely proportional to the square of the average crystalline size by the following Eq. (3).

$$\delta = \frac{1}{D^2} \tag{3}$$

where, *D* is the average crystalline size of the SnO_2 NPs. The obtained results revealed that the dislocation density is slightly higher for co-doped one compeering to un-doped and single-doped samples (See Table 1). This may be due to an increase in the occurrence of grain boundaries because of crystalline size reduction with increasing dopant concentrations. The micro-strain (ε) can be calculated by the following Eq. (4) [47].

$$\varepsilon = \frac{\beta}{4\tan\theta} \tag{4}$$

where, β is FWHM and θ is diffraction angle. From Table 1, the result shows that the micro-strain of the sample has increased from 8.8026×10^{-3} to 12.6982×10^{-3} with the reduction of the crystallite size of the SnO_2 NPs.

3.2 Surafce morphology analysis

The surface morphology of the prepared un-doped, singly doped, and co-doped samples was studied using SEM. The SEM images confirmed that all the prepared samples were well-crystallized and also that they were uniform, spherical, and aggregated as shown in Fig. 3a–c. Each sample's grains are made up of large aggregates that are transformed into fine aggregates as the dopant concentration increased. From Fig. 3a, it is observed that un-doped samples show aggregate forms. During the synthesis process, the aggregated shapes exist through strong hydrogen bonding in the precipitate [48]. The singly doped and co-doped samples show spherical and aggregate morphological shapes. However, the co-doped samples show relatively smooth and dense surface compared to the undoped and singly doped samples. This suggests that there was uniform nucleation throughout the growth of SnO_2 NPs doped with Cu and Ni. This also indicates the crystalline quality of SnO_2 NPs is greatly improved by the co-doping effect. The SEM results demonstrate that the morphologies of the prepared samples were dependent on the dopant elements, indicating that Sn^{4+} ions have been replaced with dopant ions in the SnO_2 lattice. Figure 2a–c shows a particle size distribution histogram from the SEM images and it was estimated 87. 82 nm, 86.91 nm and 83.57 nm for un-doped, single-doped and co-doped samples respectively. These results are very consistent with the variations of the crystalline size calculated from XRD analysis.

3.3 EDX analysis

The EDX spectra of the prepared un-doped, singly doped, and co-doped samples are depicted in Figs. 3d–f. EDX analyses were carried out without the restriction of elements and confirmed the presence of the expected elements, Sn, Cu, Ni, and O (see Fig. 3d–f). The un-doped, singly doped, and co-doped samples in Sn/O, Sn/O/Cu, and Sn/O/Cu/Ni weight ratios of 81.43/18.23, 81.29/15.46/2.74, and 83.88/10.74/4.20/1.18, respectively, are shown in Fig. 3d–f. Furthermore, EDX investigations demonstrated that the

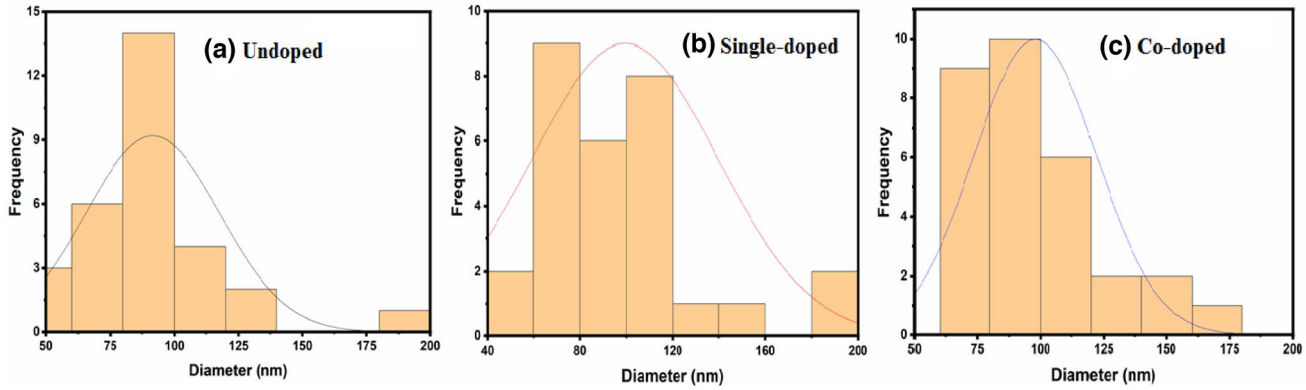

Fig. 2 A particle size distribution histogram determined from the SEM images for (**a**) un-doped, **b** 5% Cu: SnO_2 NPs, **c** 5% (Cu, Ni):SnO_2NPs

dopant elements were effectively integrated into the SnO_2 lattice without the creation of extra phases, which matched our XRD results.

3.4 FIIR analysis

The FTIR spectra were studied for information about the surface chemistry and bonding vibration of nanomaterials. As shown in Fig. 4a–e, the FTIR spectra of un-doped, singly doped, and co-doped samples were recorded in the range of 400–4000 cm^{-1}. From the Fig. 4a–e, it can be seen that the major spectra features are almost similar for all samples except variation of the intensities of the main absorption bands and a slight absorption band shift to a higher wave numbers. The peaks at 2958 and 3684 cm^{-1} correspond to the O–H stretching mode caused by absorbed water molecules.

The broad region at 600–660 cm^{-1} was attributed to Sn–O–Sn vibrational stretching [49, 50], while the peak at 1040 cm^{-1} corresponded to the Sn-OH stretching vibration modes [51]. The peaks of Ni–O–Sn and Cu–O–Sn are not seen clearly, which might be due to the low doping of Ni and Cu in the prepared samples. From the FTIR spectra, it was noticed a slight peak shift toward higher wave numbers with an increasing of dopants concentrations. This peak shift confirmed the appropriate incorporation of dopants atoms in to the host material [52].

The peak intensity increased for singly–doped samples compared to undoped and co-doped samples due to the formation of the Cu–Sn solid solution or the stress created by the defect phase. The presence of the SnO_2 stretching mode and the absence of Ni and Cu oxide related modes further supports the idea that Ni^{2+} and Cu^{2+} ions are successfully doped into the SnO_2 crystal structure.

3.5 UV–Vis and energy gap calculation

The reflectance spectra of the un-doped, singly doped and co-doped samples in the wavelength range of 320 nm to 800 nm are shown in Fig. 5f. All the samples showed minimum reflectance in the UV region. This could be due to charge transfer from the valence band to the conduction band in SnO_2 NPs [49]. However, the reflectance increases for all samples in the visible region, and the un-doped samples still have a better reflectance in this region. The optical band gap of the synthesized samples was calculated using the Tauc relation:

$$F(R).hv = A\left(hv - E_g\right)^n \tag{5}$$

where $F(R)$ is the Kubelka–Munk function which related to the absorption coefficient and reflectance, hv is energy of the photon E_g is the optical band gap of the material; n is depend on the nature of the transition and in the present case n was taken 1/2 for direct allowed transition. Where, R the diffuse reflectance and calculated using the kubelka–Munk function $F(R)$ using the following relation:

$$F(R) = \frac{(1-R)^2}{2R} \tag{6}$$

From Fig. 5a–e, it is observed that the average band gap values were varied from 3.38 eV to 3.65 eV with dopants concentrations. The optical band gap of un-doped samples is reduced from 3.38 eV to 3.26 eV ($\Delta E_g \approx 0.12$ eV), 3.33 eV ($\Delta E_g \approx 0.05$ eV) and 3.34 eV ($\Delta E_g \approx 0.08$ eV) for (3% Ni + 5% Cu):SnO_2, (1% Ni + 5% Cu):SnO_2 and 5% Cu: SnO_2 NPs, respectively (see Fig. 5a–d). These reduced band gaps (red shift) come from negative and positive corrections in the conduction and valence bands, respectively, by changing the sp–d exchange interactions between the band electrons

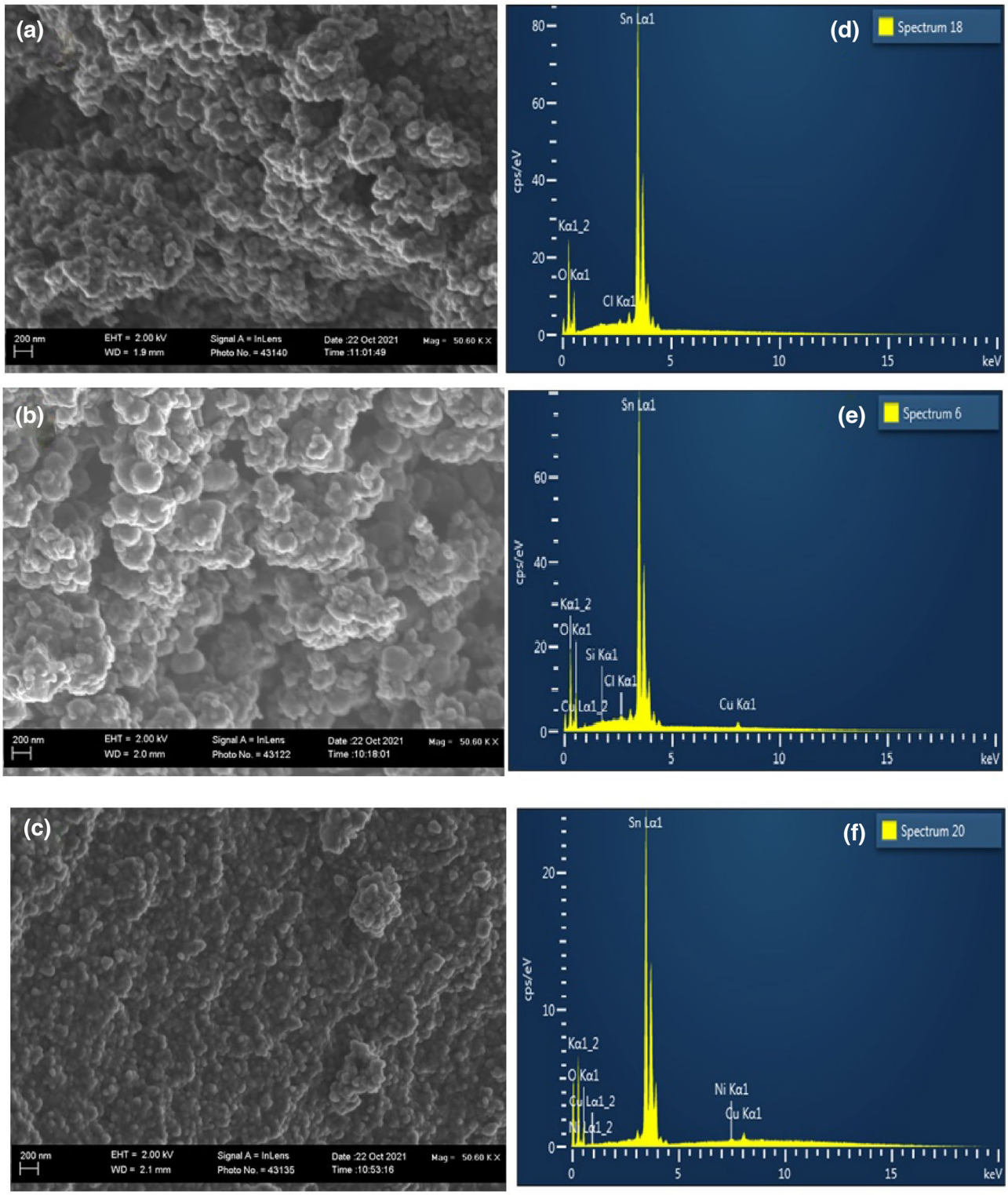

Fig. 3 SEM images of (**a**) un-doped, **b** 5% Cu:SnO_2, **c** 5% (Cu, Ni):SnO_2NPs, and EDX images of (**d**) un-doped, **e** 5% Cu:SnO_2 and **f** 5% (Cu, Ni):SnO_2NPs

and the localized d-electrons of the Ni^{2+} ions and Cu^{2+} ions [53].

This also happens when Cu^{2+} and Ni^{2+} ions substitute the Sn^{4+} ion site due to structural defects in the interstitial of Sn^{4+} or oxygen vacancies [38]. Moreover, the reduction

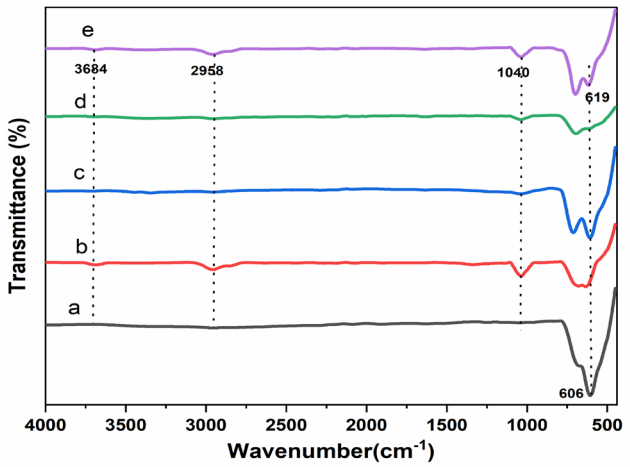

Fig. 4 FTIR spectra of (**a**) Un-doped, **b** 5% Cu:SnO_2, **c** (1% Ni + 5% Cu):SnO_2, **d** (3%Ni + 5%Cu):SnO_2,and **e** 5% (Ni, Cu): SnO_2NPs

in the band gap is the creation of new energy levels between the conduction band and the valence band due to the Ni and Cu ions in the SnO_2 host [54]. Therefore, the electronic transition happens from the filled valence band to the energy levels of defects, rather than the conventional electronic transition from the filled valence band to the empty conduction band due to the higher number of defects in the SnO_2 host site [55]. Additionally, due to the quantum confinement effect and the size effect, the band gap can be reduced by doping Cu and Cu/Ni co-doping into SnO_2 NPs [55, 56]. Furthermore, these which might be attributed to comparable ionic radii between the host and dopants of Ni and Cu ions. However, the band gap increased from 3.26 eV for (3% Ni + 5% Cu): SnO_2 to 3.65 eV for (5% Ni + 5% Cu): SnO_2 NPs. This blue shift in the band gap ($E_g \approx 0.39$ eV) is due to the increase in carrier density donated by interstitial Cu/Ni ions. The increase in carrier density shifts the Fermi level close to the conduction band, and thus the energy gap increases (Burstein–Moss effect) [56].

3.6 Photoluminescence analysis

The PL spectra of un-doped, singly doped, and co-doped samples at the excitation wavelength of 325 nm are shown in Fig. 6. The exciton spectra of the un-doped, singly doped, and co-doped samples are in the visible region. In the un-doped samples, there is one strong emission corresponding to 523 nm, along with weak bands observed at 453 nm, 476 nm, 492 nm, 494 nm, 537 nm, and 547 nm, and a broad band at 415 nm, respectively. The strong emissions peak of all co-doped samples at 512 nm was accompanied by a weak band centered at 441 nm, 481 nm, 494 nm, 525 nm, 535 nm, and a broad band at 406 nm. The singly doped shows the strong emission peaks observed at 523 nm, along with a weak band of emissions at 453 nm, 501 nm, 537 nm, and 547 nm, and a broad band at 417 nm. The violet emission peaks at 406 nm, 415 nm, and 417 nm correspond to donor–acceptor recombination because the donor levels are closest to the conduction band while the acceptor levels are at the top of the valence band [57]. Due to the emission peak energies of (3.05, 2.98, and 2.97 eV), are lower than the corresponding optical band gap energies of all the elaborated samples. The blue emission peaks centered at 441 nm and 453 nm are due to defects which are responsible for oxygen and tin vacancies [58–60].

The blue–green emission band at 476 nm, 492 nm, 481 nm, and 494 nm is due to surface defects in the SnO_2 NPs corresponding to the transition between oxygen vacancy and oxygen interstitial defect or lattice defects related to oxygen and Sn vacancies [61, 62]. Green emission peaks were found at 512 nm, 523 nm, 525 nm, 535 nm, 537 nm and 547 nm, which is attributed to the defect energy levels created by oxygen vacancies, tin interstitials and impurity Cu^{2+} and Ni^{2+} ions in the bandgap of SnO_2 NPs [63–66]. All the samples in the visible region show different emissions due to several intrinsic defects in SnO_2 NPs. The un-doped samples exhibited a strong and higher intensity as compared to the singly doped and co-doped samples. This is due to the weak interaction of the Sn–O bond in comparison to the Cu–O or Ni–O bond, and the oxygen vacancy defects are increased [68]. Moreover, the intensity of the PL peak of co-doped samples was increased as compared to singly doped samples. This is due to the increase in the density of oxygen vacancies in the band gap of co-doped SnO_2 NPs.

The intensity of the emission peaks of singly doped samples decreased. This indicates that the excited electrons are trapped by the oxygen vacancies and holes by dopant Cu ions [68]. Moreover, the excited electrons can migrate from the valance band to the new energy levels introduced nearer to the conduction band by cu-doping, which reduces the PL intensity [68]. The small shift in peak position toward shorter wavelengths (higher energy) is due to the substitution of doping ions, and it can be found in the blue shift of the energy gap with co-doping as shown in Fig. 6a–e. The most common defect that causes a new energy level within the SnO_2 band gap is oxygen vacancies, and there are three possible charge states: $V^0{}_O$, $V^+{}_O$, and $V^{++}{}_O$. In the present case, the peak at 406 nm might be due to $V_0{}^o$ states while the peak ranging from 453 to 547 nm is due to $V_0{}^+$, and $V_0{}^{++}$ states. Oxygen vacancies and structural flaws, which are induced by electron–hole recombination in the valance band, play the most important roles in the photoluminescence emission spectrum.

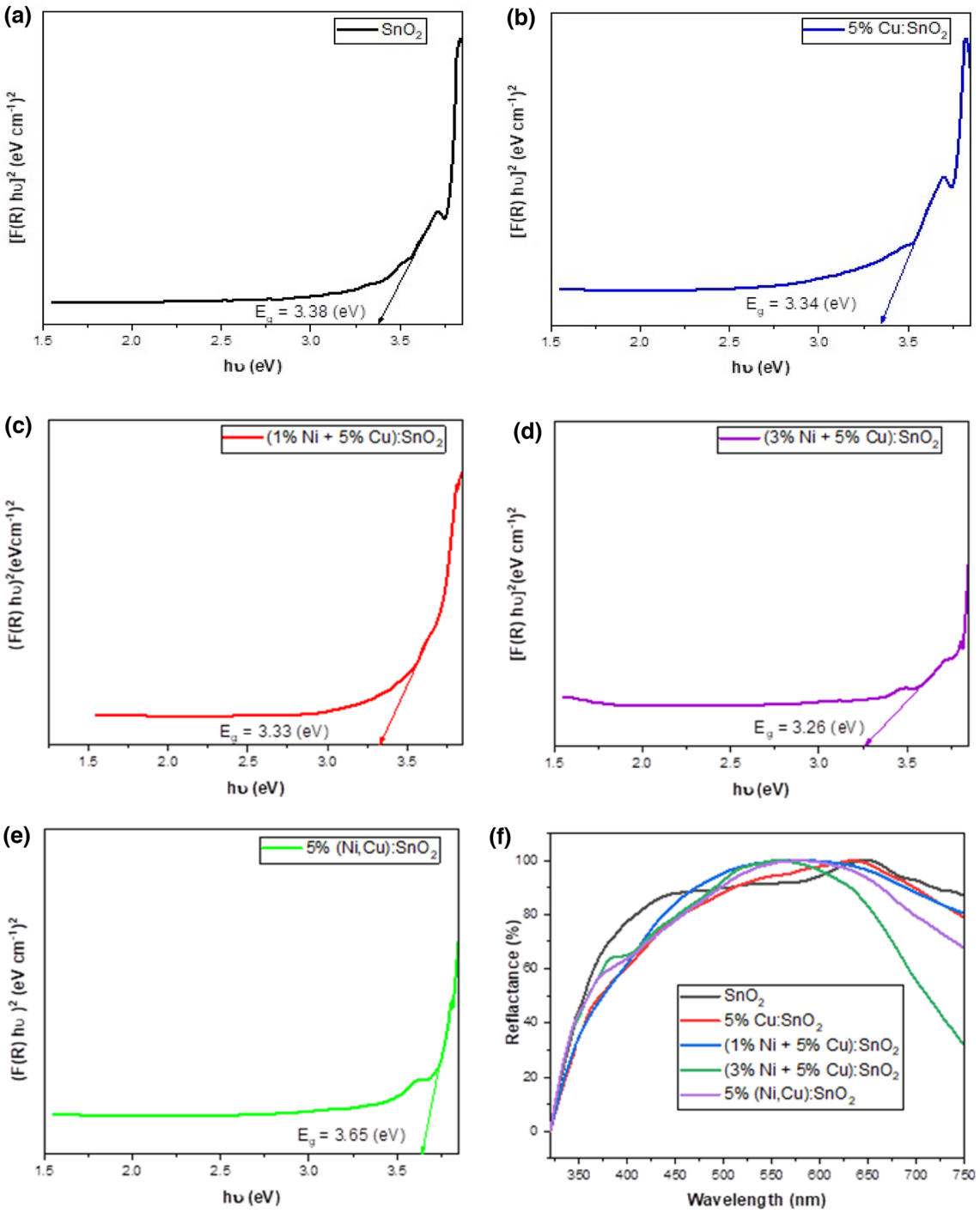

Fig. 5 The optical band gap of (**a**) un-doped, **b** 5% Cu: SnO_2, **c** (1% Ni + 5%Cu):SnO_2, **d** (3% Ni + 5% Cu):SnO_2, **e** 5% (Ni, Cu):SnO_2NPs and **f** UV–Vis diffuse reflectance spectra versus wavelength of all samples

3.7 Electrical properties analysis

The electrical properties were carried out by the temperature-dependent electrical conductivity of un-doped, singly doped, and co-doped samples by the four probe Hall effect measuring method in the temperature range of 290–350 K. As shown in Fig. 7a–c, the increase in conductivity with increasing temperature indicates that the thin film is semiconducting. The rise in conductivity of the thin films with temperature is owing to a drop in grain boundary concentration [69] and an increase in ionized defects such as oxygen vacancies [70], both of which increase charge carrier

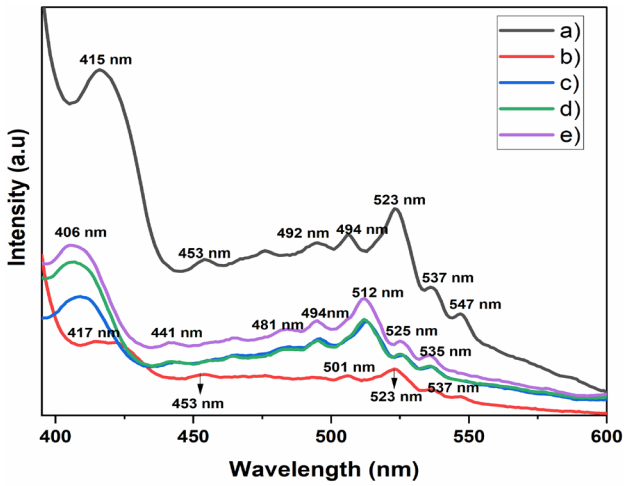

Fig. 6 Photoluminescence of spectra (**a**) un-doped, **b** 5% Cu: SnO_2 (**c**) (3% Ni + 5% Cu):SnO_2 (**d**) (1% Ni + 5% Cu):SnO_2 and **e** 5% (Cu, Ni):SnO_2 NPs

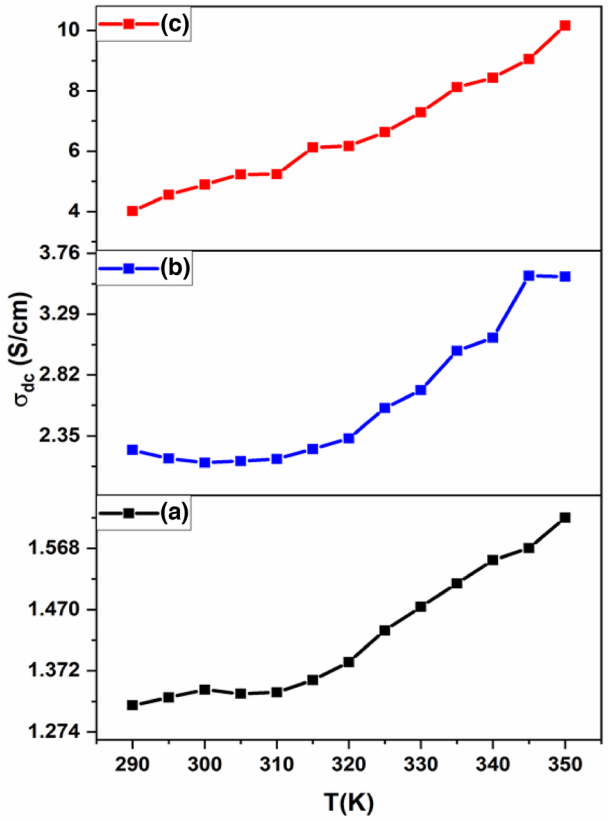

Fig. 7 Plot σ vs. T of (**a**) un-doped, **b** 5% Cu: SnO_2, **c** 5% (Cu, Ni):SnO_2 thin films

concentration and mobility [71, 72]. The following relationship can be used to analyse the conductivity using the Arrhenius equation relation (7) [73].

$$\sigma = \sigma_0 \exp\left(-\frac{\Delta E}{KT}\right) \tag{7}$$

where, ΔE is the activation energy, T is the temperature, k is the Boltzmann constant and σ_0 is the pre-exponential factor. In general, temperature-dependent total conductivity (σ_{Tot}) of a sample consists of an electronic and ionic contribution which is expressed as follows (8) [74].

$$\sigma_{Tot} = \sigma_e + \sigma_i \tag{8}$$

Where σ_e is electronic conductivity and σ_i is ionic conductivity. The activation energy values for all as-deposited films can be calculated from the slope of the arrhenius plot (lnσ versus 1000/T) in the temperature range of 290–350 K.

As shown in Fig. 8a–c, region-II has a higher activation energy than region-I. The lower activation energy of region-I suggests that electron conduction is occurring. The increase in activation energy in the higher temperature region-II leads to ionic conduction, which is the dominating electronic conduction process. The activation energy of undoped, singly doped, and co-doped thin films was calculated to be between 0.34 and 0.69 eV. The activation energy increases with increasing conductivity as temperature rises (see Fig. 8a–c); however, the co-doped SnO_2 thin film has a higher activation energy than un-doped and singly doped. This is because the co-doped SnO_2 thin film had a better surafce morphology with less surface defects.

3.7.1 I–V curve measurement

The voltage–current characteristics of un-doped, singly doped, and co-doped samples were studied under dark condition in the svoltage range of − 2 V to + 2 V as shown in

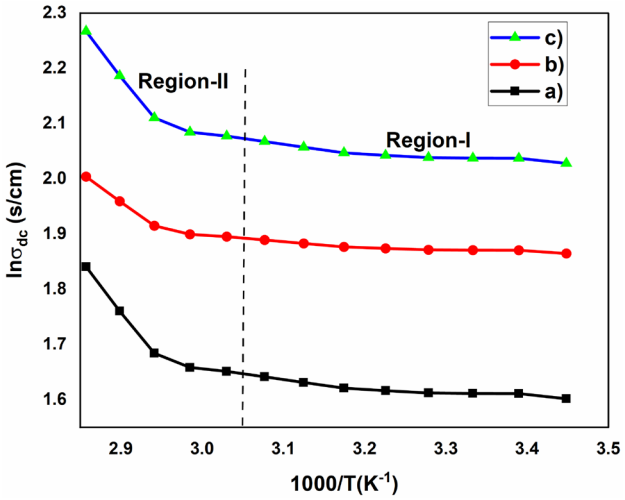

Fig. 8 Plot lnσ vs. 1000/T of a) un-doped,b) 5% Cu:SnO_2, c) 5% (Cu, Ni) co-doped SnO_2 thin films

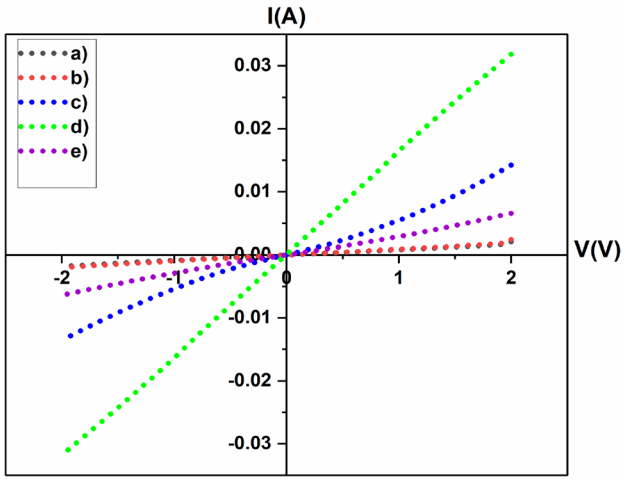

Fig. 9 I–V curves of (**a**) un-doped, **b** (1% Ni + 5% Cu: SnO_2), **c** (3% Ni + 5% Cu):SnO_2, **d** 5% (Cu, Ni):SnO_2 and **e** 5% Cu: SnO_2 thin films

Fig. 9a–e. The prepared thin films were deposited using simple spin coating method on glass substrates. Then the film was dried in an oven at 80 °C for 2 h. The contact was made over the prepared film using silver paste and again dried in oven at 120 for 30 min. The results demonstrate a linear I–V relationship under both reverse and forward bias, indicating that the investigated thin films have good ohmic contact behavior, as shown in Fig. 9 [75]. The resistivity of the sample was calculated using (9) [76].

$$\rho = \frac{RxA}{L} \tag{9}$$

where, ρ is the resistivity in (Ω. cm),R is the resistance (Ω), A is the area of active layer (cm^{-2}) and L is the length in (cm).

The estimated resistivity values are 31.39 Ω.cm, 8.69 Ω.cm and 1.65 Ω.cm for un-doped, single-doped and co-doped samples respectively. From the results, it can be clearly observed that the resistivity of the prepared materials decreased with dopants concentrations. Moreover, the result revealed that the co-doped material has a better conductivity than others. This result is consistent with the previous sections findings. This enhancement of conductivity may be due to the increase in carrier charge mobility in the doped prepared nanomaterials [75]. As a result, the electrical properties of co-doped thin films were found to be better than that of un-doped thin films. From the results, it is observed that the prepared samples show ohmic nature. All the electrical study results revealed that the prepared samples have an interesting feature for various optoelectronic applications.

4 Conclusion

Un-doped, singly doped and co-doped of samples were successfully synthesized using the sol–gel method. The effects of adding Cu and Ni on the structural, optical and electrical properties, as well as the surface morphology of SnO_2 NPs, were studied thoroughly by employing various characterization techniques. The XRD study revealed that singly doped/co-doped and un-doped samples exhibited a tetragonal rutile crystal structure with a preferred orientation along the (110) plane. The lattice parameters and the micro-strain were decreased with increasing the average crystal size. The XRD result also shows that the diffraction peak positions were shifted toward higher 2θ angel with Ni concentrations. The UV–Vis analyses revealed that the optical band gaps of the prepared samples were increased with the dopant concentrations. The SEM micrographs confirmed that the prepared samples have spherical shape and agglomerated irrespective of the concentrations of the dopants. The four–probe Hall Effect measurement justified the presence of two distinct conduction mechanisms at two distinct temperature regions. The resistivity values of the prepared thin films were decreased from 31.39 Ω.cm for un-doped to 0.43 Ω.cm for 3% Ni + 5% Cu: SnO_2 respectively. All the obtained results revealed that the prepared materials are good candidates for optoelectronic applications. Moreover, it was observed that co-doping gives another opportunity to tune the physical properties of SnO_2 NPs for various applications.

Acknowledgements The corresponding author Dr Fekadu Gahsw is acknowledge the support from Addis Ababa University thematic research project (Grant Ref. LT/PY-242/2021).

References

1. P. Pascariu Dorneanu, A. Airinei, M. Grigoras, N. Fifere, L. Sacarescu, N. Lupu, L. Stoleriu, Structural, optical and magnetic properties of Ni-doped SnO_2 nanoparticles. J. Alloy Compd. **668**, 65–72 (2016)
2. B. Venugopal, B. Nandan, A. Ayyachamy, V. Balaji, S. Amirthapandian, B.K. Panigrahi, T. Paramasivam, Influence of manganese ions in the band gap of tin oxide nanoparticles: structure, microstructure and optical studies. RSC Adv. **4**, 6141–6150 (2014)
3. V. Kumar, K. Singh, J. Sharma, A. Kumar, A. Vij, A. Thakur, Zn-doped SnO_2 nanostructures: structural, morphological and spectroscopic properties. J. Mater. Sci. Mater. **28**(24), 18849–18856 (2017)
4. M. Batzill, U. Diebold, the surface and materials science of tin oxide. Prog. Surf. Sci. **79**, 47–154 (2005)
5. M.P. Subramaniam, G. Arunachalam, R. Kandasamy, P. Veluswamy, I. Hiroya, Effect of pH and annealing temperature on the properties of tin oxide nanoparticles prepared by sol-gel method. J. Mater. Sci-Mater. El. **29**, 658–666 (2018)

6. E. Shanthi, V. Dutta, A.S. Banerjee, K.L. Chopra, Electrical and optical properties of undoped and antimony-doped tin oxide films. J. Appl. Phys. **51**(12), 6243–6251 (1980)
7. C. Mrabet, A. Boukhachem, M. Amlouk, T. Manoubi, Improvement of the optoelectronic properties of tin oxide transparent conductive thin films through lanthanum doping. J. Alloy Compd. **666**, 392–405 (2016)
8. E.J. López-Naranjo, L.J. González-Ortiz, L.M. Apátiga, E.M. Rivera-Muñoz, A. Manzano-Ramírez, Transparent electrodes: a review of the use of carbon-based nanomaterials. J Nanomater **2016**, 1 (2016)
9. D. Haridas, V. Gupta, Enhanced response characteristics of SnO_2 thin film based sensors loaded with Pd clusters for methane detection. Sens. Actuat. B:Chem **166**, 156–164 (2012)
10. E.T.H. Tan, G.W. Ho, A.S.W. Wong, S. Kawi, A.T.S. Wee, Gas sensing properties of tin oxide nanostructures synthesized via a solid-state reaction method. Nanotechnology **19**(25), 255706 (2008)
11. A. Papaderakis, I. Mintsouli, J. Georgieva, S. Sotiropoulos, Electrocatalysts prepared by galvanic replacement. Catalysts **7**(3), 80 (2017)
12. A.M.A. Maisara, M.K. Khairudin, H. Lee, A.R. Sheikh, Synthesis of tin oxide nanostructures using hydrothermal method and optimization of its crystal size using statistical design of experiment. Procedia Chem. **19**, 993–998 (2016)
13. P. Baraneedharan, S.I. Hussain, V.P. Dinesh, C. Siva, P. Biji, M. Sivakumar, Lattice doped Zn-SnO_2 nanospheres: a systematic exploration of dopant ion effects on structural, optical, and enhanced gas sensing properties. Appl. Surf. Sci. **357**, 1511–1521 (2015)
14. A.-M. Ungureanu, O. Oprea, B.S. Vasile, C. Andronescu, G. Voicu, I. Jitaru, Temperature effect over structure and photochemical properties of nanostructured SnO_2 powders. Cent. Eur. J. Chem. **12**, 909–917 (2014)
15. M. Ivanovskaya, E. Ovodok, V. Golovanov, The nature of paramagnetic defects in tin (IV) oxide. Chem. Phys. **457**, 98–105 (2015)
16. G. Singh, R.C. Singh, Synthesis and characterization of Gd-doped SnO_2 nanostructures and their enhanced gas sensing properties. Ceram Int. **43**, 2350–2360 (2017)
17. C. Fu, J. Wang, M. Yang, X. Su, J. Xu, B. Jiang, Effect of La doping on microstructure of SnO_2 nanopowders prepared by coprecipitation method. J. Non-Cryst Solids. **357**, 1172–1176 (2011)
18. M. Akram, A.T. Saleh, W.A.W. Ibrahim, A.S. Awan, R. Hussain, Continuous microwave flow synthesis (CMFS) of nano-sized tin oxide: Effect of precursor concentration. Ceram Int **42**, 8613–8619 (2016)
19. S.M. Priya, A. Geetha, K. Ramamurthi, Structural, morphological and optical properties of tin oxide nanoparticles synthesized by sol-gel method adding hydrochloric acid. J. Sol-Gel Sci. Technol. **78**, 365–372 (2016)
20. A.G. Habte, F.G. Hone, F.B. Dejene, Effect of solution pH on structural, optical and morphological properties of SnO_2 nanoparticles. Phys. B: Condens. Matter. **580**, 411832 (2020)
21. A.K. Singh, V. Viswanath, V.C. Janu, Synthesis, effect of capping agents, structural, optical and photoluminescence properties of ZnO nanoparticles. J. Lumin. **129**(8), 874–878 (2009)
22. R. Adhikari, A.K. Das, D. Karmakar, T.C. Rao, J. Ghatak, Structure and magnetism of Fe-doped SnO_2 nanoparticles. Phys. Rev. B. **78**(2), 02440 (2008)
23. H. Jin, Y. Xu, G. Pang, W. Dong, Q. Wan, F.S. SunY, Al-doped SnO_2 nanocrystals from hydrothermal systems. Mater. Chem. Phys. **85**(1), 58–62 (2004)
24. N. Salah, S. Habib, A. Azam, M.S. Ansari, W.M. Al-Shawafi, Formation of Mn-doped SnO_2 nanoparticles via the microwave technique: structural, optical and electrical properties. Nanomater. Nanotech. **6**, 17 (2016)
25. X. Xu, Y. Tong, J. Zhang, X. Fang, J. Xu, F. Liu, J. Liu, W. Zhong, O.E. Lebedeva, X. Wang, Investigation of lattice capacity effect on Cu^{2+}doped SnO_2 solid solution catalysts to promote reaction performance toward NO_x-SCR with NH_3. Chinese J. Catal. **41**(5), 877–888 (2020)
26. M. Kuppan, S. Kaleemulla, N. MadhusudhanaRao, N. SaiKrishna, Structural, optical and magnetic properties of Ni-doped SnO_2 thin films prepared by flash evaporation technique. Int. J. ChemTech Res. **6**(3), 1933–1935 (2014)
27. A. Bouaine, N. Brihi, G. Schmerber, C. Ulhaq-Bouillet, S. Colis, A. Dinia, Structural, optical, and magnetic properties of Co-doped SnO_2 powders synthesized by the coprecipitation technique. J. Phys. Chem. **111**(7), 2924–2928 (2007)
28. J. Divya, A. Pramothkumar, S.J. Gnanamuthu, D.B. Victoria, Structural, optical, electrical and magnetic properties of Cu and Ni doped SnO_2 nanoparticles prepared via Co-precipitation approach. Phys. B: Condens. Matter. **588**, 412169 (2020)
29. M.A. Basyooni, Y.R. Eker, M. Yilmaz, Structural, optical, electrical and room temperature gas sensing characterizations of spin coated multilayer cobalt-doped tin oxide thin films. Superlattice Micro **140**, 106465 (2020)
30. S. Nilavazhagan, S. Muthukumaran, Investigation of optical and structural properties of Fe, Cu co-doped SnO_2 nanoparticles. Superlattice Micro **83**, 507–520 (2015)
31. S. Bhuvana, H.B. Ramalingam, G. Thilakavathi, K. Vadivel, Structural, optical and magnetic properties of (Ni-Mn) co-doped tin oxide nanoparticles. Mater Technol. **32**, 305–309 (2017)
32. S. Mehraj, M. Shahnawaze Ansari, Alimuddin, Structural, electrical and magnetic properties of (Fe, Co) co-doped SnO_2 diluted magnetic semiconductor nanostructures. Phys. E. **65**, 84–92 (2015)
33. P.V. Reddy, S.V. Reddy, B.S. Reddy, Synthesis and properties of (Fe, Al) codoped SnO_2 nanoparticles. Mater Today: Proc. **3**, 1752–1761 (2016)
34. N. Houaidji, M. Ajili, B. Chouial, N.T. Kamoun, First investigation of structural and optoelectronic properties of F and Ni co-doped SnO_2 sprayed thin films. Optik **208**, 164026 (2020)
35. N. Ahmad, S. Khan, Effect of (Mn-Co) co-doping on the structural, morphological, optical, photoluminescence and electrical properties of SnO_2. J. Alloys Compd. **720**, 502–509 (2017)
36. M. Duhan, N. Kumar, A. Gupta, A. Singh, H. Kaur, Enhanced room temperature ferromagnetism in Cr and Fe co-doped SnO_2 nanoparticles synthesized by sol-gel method. Vacuum **181**, 109635 (2020)
37. R. Ramarajan, M. Kovendhan, K. Thangaraju, D.P. Joseph, R.R. Babu, V. Elumalai, Enhanced optical transparency and electrical conductivity of Ba and Sb co-doped SnO_2 thin films. J. Alloy Compd. **823**, 153709 (2020)
38. J. Divya, A. Pramothkumar, H.J.L. Hilary, P.J. Jayanthi, P.C. Jobe brabakar, Impact of copper (Cu) and iron (Fe) co-doping on structural, optical, magnetic and electrical properties of tin oxide (SnO_2) nanoparticles for optoelectronics applications. J Mater Sci: Mater. Electron. **32**, 16755–16785 (2021)
39. N. Lavanya, C. Sekar, E. Fazio, F. Neri, S.G. Leonardi, G. Neri, Development of a selective hydrogen leak sensor based on chemically doped SnO_2 for automotive applications. Int. J. Hydrog. Energy. **42**(15), 10645–10655 (2017)
40. S. Zulfiqar, Z. Iqbal, J. Lü, Zn-Cu-codoped SnO_2 nanoparticles: structural, optical, and ferromagnetic behaviors. Chin. Phys. B. **26**, 126104 (2017)
41. M. Ashokkumar, S. Muthukumaran, Microstructure, optical and FTIR studies of Ni, Cu co-doped ZnO NPs by co-precipitation method. Opt. Mater. **37**, 671–678 (2014)

42. B. Babu, A.N. Kadam, R.V.S.S.N. Ravikumar, C. Byon, Enhanced visible light photocatalytic activity of Cu-doped SnO_2 quantum dots by solution combustion synthesis. J. Alloy Compd. **703**, 330–336 (2017)
43. A. Abdelkrim, S. Rahmane, O. Abdelouahab, N. Abdelmalek, G. Brahim, Effect of solution concentration on the structural, optical and electrical properties of SnO_2 thin films prepared by spray pyrolysis. Optik **127**, 2653–2658 (2016)
44. P.K. Sharma, R.K. Dutta, A.C. Pandey, Effect of nickel doping concentration on structural and magnetic properties of ultrafine diluted magnetic semiconductor ZnO nanoparticles. J. Magn. Magn. **321**(20), 3457–3461 (2009)
45. S. Thanikaikarasan, K. Sundaram, T. Mahalingam, S. Velumani, J.K. Rhee, Electrodeposition and characterization of Fe doped CdSe thin films from aqueous solution. Mater. Sci. Eng. **174**(1–3), 242–248 (2010)
46. E.T. Seid, F.B. Dejene, Z.N. Urgessa, J.R. Botha, Refluxed sol–gel synthesized ZnO nanopowder with variable zinc precursor concentration. Appl. Phys. A **124**(11), 738 (2018)
47. B. Rajesh Kumar, B. Hymavathi, X-ray peak profile analysis of solid-state sintered alumina doped zinc oxide ceramics by Williamson-Hall and size-strain plot methods. J. Asian Ceram. Soc. **5**(2), 94–103 (2017)
48. P.V. Reddy, S.V. Reddy, B.S. Reddy, Synthesis and properties of (Fe, Al) co-doped SnO_2 nanoparticles. Mater. Today: Proc. **3**(6), 1752–1761 (2016). (**Eram Soc .5: 94–103**)
49. N. Sergent, P. Gélin, L. Périer-Camby, H. Praliaud, G. Thomas, Preparation and characterisation of high surface area stannic oxides: structural, textural and semiconducting properties. Sensor Actuat. B- Chem. **84**, 176–188 (2002)
50. N. Ahmad, S. Khan, Effect of (Mn-Co) co-doping on the structural, morphological, optical, photoluminescence and electrical properties of SnO_2. J. Alloy Compd. **720**, 502–509 (2017)
51. M. Shu, X. Li, Electrospun MnxCo0.5−xSn0.5O2 and SnO2 porous nanofibers and nanoparticles as anode materials for lithium-ion battery. J Nanopart Res. **21**, 179 (2019)
52. F.G. Hone, F.B. Dejene, L.F. Koao, Tailoring optical and electrical properties of ternary $Pb_{1-x}Co_xS$ thin films synthesized from a combination of two complexing agents. Indian J. Phys **95**(9), 1763–1773 (2021)
53. K.J. Kim, Y.R. Park, Spectroscopic ellipsometry study of optical transitions in Zn 1–x Cox O alloys. Appl. Phys. Lett. **81**(8), 1420–1422 (2002)
54. A.G. Habte, F.G. Hone, F.B. Dejene, Zn doping effect on the properties of SnO_2 nanostructure by co-precipitation technique. Appl. Phys. A **125**, 402 (2019)
55. P. Baraneedharan, S.I. Hussain, V.P. Dinesh, C. Siva, P. Biji, M. Sivakumar, Lattice doped Zn–SnO_2 nanospheres: a systematic exploration of dopant ion effects on structural, optical, and enhanced gas sensing properties. Appl. Surf. Sci. **357**, 1511–1521 (2015)
56. S. Suwanboon, T. Ratana, T. Ratana, Effects of Al and Mn dopant on structural and optical properties of ZnO thin film prepared by sol-gel route. Walailak J. Sci. Technol. **4**(1), 111–121 (2007)
57. S. Bansal, D.K. Pandya, S.C. Kashyap, D. Haranath, Growth ambient dependence of defects, structural disorder and photoluminescence in SnO_2 films deposited by reactive magnetron sputtering. J. Alloys Compd. **583**, 186–190 (2014)
58. A. Kar, A. Patra, Optical and electrical properties of Eu^{3+}-doped SnO_2 nanocrystals. J. Phys. Chem. C. **113**(11), 4375–4380 (2009)
59. E.J. Lee, C. Ribeiro, T.R. Giraldi, E. Longo, E.R. Leite, J.A. Varela, Photoluminescence in quantum-confined SnO_2 nanocrystals: evidence of free exciton decay. Appl. Phys. Lett. **84**(10), 1745–1747 (2004)
60. W.S.F. GuF, M.K. Lü, X.F. Cheng, S.W. Liu, G.J. Zhou, D.R. Yuan, Luminescence of SnO_2 thin films prepared by spin-coating method. J. Cryst. Growth **262**(1–4), 182–185 (2004)
61. F. Gu, S.F. Wang, M.K. Lü, G.J. Zhou, D. Xu, D.R. Yuan, Photoluminescence properties of SnO_2 nanoparticles synthesized by sol− gel method. J. Phys. Chem **108**(24), 8119–8123 (2004)
62. A.S.H. Hameed, C. Karthikeyan, A.P. Ahamed, N. Thajuddin, N.S. Alharbi, S.A. Alharbi, G. Ravi, In vitro antibacterial activity of ZnO and Nd- doped ZnO nanoparticles against ESBL producing Escherichia coli and Klebsiella pneumoniae. Sci. Rep. **6**(1), 1–11 (2016)
63. R.K. Mishra, A. Kushwaha, P.P. Sahay, Influence of Cu doping on the structural, photoluminescence and formaldehyde sensing properties of SnO_2 nanoparticles. RSC Adv. **4**(8), 3904–3912 (2014)
64. C.T. Lee, Fabrication methods and luminescent properties of ZnO materials for light-emitting diodes. Mater. **3**(4), 2218–2259 (2010)
65. I. AlivovY, M.V. Chukichev, V.A. Nikitenko, Green luminescence band of zinc oxide films copper-doped by thermal diffusion. J. Semicond. **38**(1), 31–35 (2004)
66. F.H. Leiter, H.R. Alves, A. Hofstaetter, D.M. Hofmann, B.K. Meyer, Rapid research notes-the oxygen vacancy as the origin of a green emission in undoped ZnO. Phys. Status Solidi. **226**(1), R4 (2001)
67. A. Rahmati, A.B. Sirgani, M. Molaei, M. Karimipour, Cu-doped ZnO nanoparticles synthesized by simple co-precipitation route. Eur Phys J Plus. **129**, 250 (2014)
68. N. Shanmugam, T. Sathya, G. Viruthagiri, C. Kalyanasundaram, R. Gobi, S. Ragupathy, Photocatalytic degradation of brilliant green using undoped and Zn doped SnO_2 nanoparticles under sunlight irradiation. Appl. Surf. Sci. **360**, 283–290 (2016)
69. D. Das, R. Banerjee, Properties of electron-beam-evaporated tin oxide films. Thin Solid Films **147**(3), 321–331 (1987)
70. J. Bruneaux, H. Cachet, M. Froment, A. Messad, Correlation between structural and electrical properties of sprayed tin oxide films with and without fluorine doping. Thin Solid Films **197**(1–2), 129–142 (1991)
71. H. Sefardjella, B. Boudjema, A. Kabir, G. Schmerber, Structural and photoluminescence properties of SnO_2 obtained by thermal oxidation of evaporated Sn thin films. Curr. Appl. Phys. **13**(9), 1971–1974 (2013)
72. J.H. Bang, N. Lee, A. Mirzaei, M.S. Choi, H.G. Na, C. Jin, H.W. Kim, Effect of microwave irradiation on the electrical and optical properties of SnO_2 thin films. Ceram Int. **45**(6), 7723–7729 (2019)
73. F. Yakuphanoglu, Electrical conductivity, Seebeck coefficient and optical properties of SnO_2 film deposited on ITO by dip coating. J. Alloys Compd. **470**(1–2), 55–59 (2009)
74. J.L.G. Fierro, Metal oxides: chemistry and applications. Mater. Today. **8**(12), 59 (2005)
75. L. Soussi, T. Garmim, O. Karzazi, A. Rmili, A. El Bachiri, A. Louardi, H. Erguig, Effect of (Co, Fe, Ni) doping on structural, optical and electrical properties of sprayed SnO_2 thin film. Surf. Interfaces. **19**, 100467 (2020)
76. F.G. Hone, N.A. Tegegne, F.B. Dejene, D.M. Andoshe, Nanofiber cadmium oxide thin films prepared from ethanolamine complexing agent by solution growth method. Optik **243**, 167402 (2021)